

# Doubly resonant second-harmonic generation in a fiber-based tunable open microcavity

Xinhang Kong (孔欣航)<sup>1</sup>, Zhuojun Liu (刘卓俊)<sup>2\*</sup>, Lijun Song (宋丽军)<sup>1</sup>, Guixin Qiu (邱贵鑫)<sup>1</sup>, Xuying Wang (王栩莹)<sup>1</sup>, Jiantao Ma (马剑涛)<sup>1</sup>, Dunzhao Wei (魏敦钊)<sup>1\*\*</sup>, and Jin Liu (刘进)<sup>1</sup>

<sup>1</sup>State Key Laboratory of Optoelectronic Materials and Technologies, School of Physics, Sun Yat-sen University, Guangzhou 510275, China

<sup>2</sup>State Key Laboratory for Mesoscopic Physics and Frontiers Science Center for Nano-optoelectronics, School of Physics, Peking University, Beijing 100871, China

\*Corresponding author: [zhuojunliu@pku.edu.cn](mailto:zhuojunliu@pku.edu.cn)

\*\*Corresponding author: [weidzh@mail.sysu.edu.cn](mailto:weidzh@mail.sysu.edu.cn)

Received June 6, 2023 | Accepted June 26, 2023 | Posted Online November 1, 2023

Microcavities constructed from materials with a second-order nonlinear coefficient have enabled efficient second-harmonic (SH) generation at a low power level. However, it is still technically challenging to realize double resonance with large nonlinear modal overlap in a microcavity. Here, we propose a design for a robust, tunable, and easy coupling double-resonance SH generation based on the combination of a newly developed fiber-based Fabry-Perot microcavity and a sandwich structure, whose numerical SH conversion efficiency is up to 3000%  $W^{-1}$ . This proposal provides a feasible way to construct ultra-efficient nonlinear devices for generation of classical and quantum light sources.

**Keywords:** microcavity; double resonance; second-harmonic generation.

**DOI:** [10.3788/COL202321.11901](https://doi.org/10.3788/COL202321.11901)

## 1. Introduction

Cavity-enhanced second-order nonlinearities refer to nonlinear interactions between light and materials when second-order nonlinear processes ( $\chi^{(2)}$ ) happen inside a cavity, which have been widely used to generate wavelength-tunable laser sources from violet to terahertz (THz) waves and high-quality quantum entanglement sources<sup>[1-5]</sup>. With the availability of various low-loss thin-film platforms ranging from CMOS-compatible silicon nitride (SiN) and III-V compound semiconductor to emerging aluminum nitride and lithium niobate (LN), optical microcavities with different geometries have been minimized on chip through advanced nanofabrication techniques. These microcavities mainly include microrings or microdisks based on whispering gallery modes (WGMs), photonic crystal defect using bandgap modes, and photonic crystal slabs with bound states in the continuum (BIC), enabling long-time confinement of light in a small volume to enhance  $\chi^{(2)}$  nonlinear processes, especially for second-harmonic generation (SHG)<sup>[6-12]</sup>. In comparison to bulk cavities, small mode volume in microcavities enables higher conversion efficiency at lower power levels owing to a strong confinement of light, which is the unique advantage of microcavities in nonlinear optics. The conversion efficiency normalized to the pump power is commonly used as a criterion to characterize the low-power-consumption SHG. To maximize the SHG efficiency in a microcavity, it is required to

simultaneously achieve frequency matching and large nonlinear modal overlap for the fundamental-harmonic (FH) and second-harmonic (SH) waves<sup>[13,14]</sup>.

Microring or microdisk cavities with large footprints are widely used to implement multiply resonant  $\chi^{(2)}$  processes due to their high  $Q$ -factors and abundant resonant modes<sup>[15-20]</sup>. The nonlinear modal overlap around the azimuth direction in these cavities becomes a phase-matching condition because of the traveling-wave property, which should be achieved through modal phase matching or quasi-phase matching<sup>[21]</sup>. For instance, periodically poled  $z$ -cut LN microrings based on quasi-phase matching presented a record-high SHG efficiency of 250,000%  $W^{-1}$ <sup>[22]</sup>, while the modal phase matching, without requirement of technically challenging domain engineering, presented a relatively small SHG efficiency of 1500%  $W^{-1}$  owing to much smaller nonlinear modal overlap<sup>[23]</sup>. However, the mode volumes of WGM-based cavities are relatively large, which limits the achievable SHG efficiency. Alternatively, photonic crystal defect cavities feature a high  $Q$ -factor and a wavelength-scale mode volume to realize ultra-strong nonlinear light and matter interaction, but it is difficult to simultaneously design two octave-separating bandgap modes for doubly resonant SHG<sup>[24]</sup>. This difficulty is also encountered by BIC-based photonic slab cavities, although their single resonance has been used<sup>[25,26]</sup>. Therefore, a combination of the bandgap mode and

the BIC mode was proposed to realize doubly resonant SHG with a conversion efficiency up to  $2.4 \times 10^{-2} W^{-1}$ [27]. Even so, geometrically sensitive frequency matching requires the introduction of additional thermal or electrical tuning components, making the practical fabrication process more complicated[28–30].

Here, we turn to fiber-based open microcavities for designing doubly resonant SHG, which could be easily constructed by a concave mirror on an optical fiber tip facing a flat mirror with a  $\chi^{(2)}$  material inside. Fiber-based open microcavities, featuring a high  $Q$ -factor, a microscale mode volume, easy coupling with optical fibers, and tunable resonance, have been used to study optical sensing and cavity quantum electrodynamics[31–34]. By introducing an LN thin film to provide parametric gain, a SiN layer to tune frequency matching, and a silicon dioxide (SiO<sub>2</sub>) layer to maximize the modal overlap, we comprehensively study doubly resonant SHG for the microcavity. The numerical simulation results show that the SH conversion efficiency reaches up to 3000%  $W^{-1}$  for a cavity length of 1.94  $\mu\text{m}$  at the designed FH wavelength of 1310 nm, while macroscopically modifying the cavity length can adjust operation wavelength. The unique large-range and flexible tunability along with easy combination with thin-film platforms provides a practical way to construct nonlinear microcavities with multiple resonances for realizing highly efficient cavity-enhanced  $\chi^{(2)}$  processes.

## 2. Design of Fiber-Based FP Nonlinear Microcavity

As shown in Fig. 1, the fiber-based Fabry–Perot (FP) microcavity is constructed by aligning a concave distributed Bragg reflector (DBR) mirror on the tip of a single-mode optical fiber and a plane DBR mirror on a fused silica substrate. The DBR mirrors are formed by alternating stacks of TiO<sub>2</sub> and SiO<sub>2</sub> layers, whose reflection bandwidths and reflectivity for the FH and SH waves are modulated by optimizing the stack pairs and periods. The

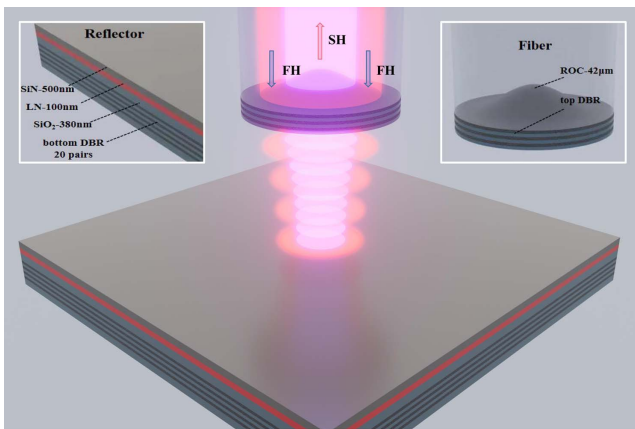


**Fig. 1.** Illustration of the fiber-based FP microcavity for doubly resonant SHG. The right inset shows a zoomed-in view of the top DBR mirror on the tip of a single-mode optical fiber. The left inset shows a zoomed-in view of the bottom DBR mirror on a fused silica substrate.

DBR mirror in our work has also been named a FASH mirror, the abbreviated form of “fundamental and SH mirror”, to present its feature of high reflectivity for both FH and SH waves, which has been used to enhance SHG from two-dimensional materials or nonlinear crystals[33,35,36]. The thicknesses of the TiO<sub>2</sub> and SiO<sub>2</sub> layers are given by  $h_{\text{TiO}_2} = (1 - \alpha)\lambda / (2n_{\text{TiO}_2})$  and  $h_{\text{SiO}_2} = \alpha\lambda / (2n_{\text{SiO}_2})$ , where  $\alpha = \frac{1}{2\pi} \arccos(-\frac{1}{3}) = 0.304$  is the optimal ratio for the FASH mirror[35]. The stack pairs on the fiber tip ( $N_{\text{top}}$ ) are always less than that on the fused silica substrate ( $N_{\text{bottom}}$ ), ensuring the considerable optical field to be in- and out-coupling via the optical fiber. For doubly resonant SHG, it is crucial to ensure that the FH and SH wavelengths satisfy the standing wave condition, expressed as

$$\begin{cases} 2\pi m_{\text{FH}} = \frac{2\pi}{\lambda_{\text{FH}}} (n_{\text{SiO}_2, \text{FH}} H_{\text{SiO}_2} + n_{\text{SiN, FH}} H_{\text{SiN}} + n_{\text{LN, FH}} H_{\text{LN}} + L_{\text{air}}) \\ \quad + \varphi_{\text{top, FH}} + \varphi_{\text{bottom, FH}} \\ 2\pi m_{\text{SH}} = \frac{2\pi}{\lambda_{\text{SH}}} (n_{\text{SiO}_2, \text{SH}} H_{\text{SiO}_2} + n_{\text{SiN, SH}} H_{\text{SiN}} + n_{\text{LN, SH}} H_{\text{LN}} + L_{\text{air}}) \\ \quad + \varphi_{\text{top, SH}} + \varphi_{\text{bottom, SH}} \end{cases}, \quad (1)$$

where  $n$  and  $H$ , whose first and second subscripts refer to the corresponding materials and frequencies, represent the refractive index and thickness, respectively. The total cavity length is given by  $L = L_{\text{SiO}_2} + L_{\text{SiN}} + L_{\text{LN}} + L_{\text{air}}$ , where  $L_{\text{air}}$  is air-gap length for the microcavity.  $\varphi_{\text{top}}$  and  $\varphi_{\text{bottom}}$  are extra phase shifts induced by the top FASH and bottom FASH mirrors, respectively.  $\lambda_{\text{FH}}$  and  $\lambda_{\text{SH}}$  are the wavelengths, while  $m_{\text{FH}}$  and  $m_{\text{SH}}$  are longitudinal mode numbers, for the resonant FH and SH modes. Considering the resonant wavelength bandwidths, one can use the figure of merit (FOM) to assess the frequency matching, given by[37]

$$\text{FOM} = \left| \frac{\lambda_{\text{FH}} - 2\lambda_{\text{SH}}}{\lambda_{\text{FH}}} \right|. \quad (2)$$

The critical frequency-matching condition, i.e.,  $\lambda_{\text{FH}} - 2\lambda_{\text{SH}} = 0$  is satisfied when  $\text{FOM} = 0$ . A sandwich structure, consisting of an additional SiO<sub>2</sub> layer, the  $x$ -cut thin-film LN with the crystal axis along the  $y$  axis, and SiN, is fixed on the plane FASH mirror to comprehensively optimize the double resonance, frequency matching, and nonlinear modal overlap, as shown in the inset of Fig. 1. The FH beam is coupled into the microcavity from the optical fiber through the concave FASH mirror and forms a standing wave. Orienting its polarization along the crystal axis of the LN, the cavity-enhanced FH field could efficiently excite SH resonance by using the maximum second-order nonlinear coefficient  $d_{33}$ . The SiN layer above the LN assists realization of critical frequency matching by compensating material dispersion induced by the LN layer and concurrently maximizes the nonlinear modal overlap in combination with the additional SiO<sub>2</sub> layer below the LN[38]. The microcavity can be considered as a plane-concave FP cavity, where the beam waist is located at the plane mirror and can be calculated using the formula of  $\omega_0 = (\frac{\lambda}{2})^2 (LR)^{1/4}$ . Here,  $L$  represents the total cavity length, and  $R$  is the curvature radius of the concave mirror. It is evident

that increasing the cavity length or curvature radius will lead to a larger  $\omega_0$ , consequently increasing mode volume inside the nonlinear layer. It should be noted that when selecting the cavity length and curvature radius, the coupling efficiency between the microcavity and the optical fiber needs to be taken into consideration. The possible experimental realization of the sandwich structure is the following: the additional  $\text{SiO}_2$  layer with a certain thickness is deposited during the preparation of the FASH mirror; then, the commercially available  $x$ -cut LN thin film on a silicon substrate is bonded onto the  $\text{SiO}_2$  layer; after the silicon substrate is removed by grinding and wet etching, the SiN layer is deposited on the LN layer to finish the structure<sup>[39]</sup>.

### 3. Double-Resonance Optimization

In the following numerical simulation, the thicknesses of  $\text{TiO}_2$  and  $\text{SiO}_2$  layers for the FASH mirrors are set as  $h_{\text{TiO}_2} = 215.0$  nm and  $h_{\text{SiO}_2} = 136.4$  nm, respectively, to achieve high reflectivity for the FH wavelength centering at 1310 nm and the corresponding SH wavelength. The single-mode fiber is 4.6  $\mu\text{m}$  in diameter, and the concave FASH mirror on its tip has a curvature radius of  $R = 42 \mu\text{m}$ <sup>[40]</sup>. Figures 2(a) and 2(b) present the reflectivity depending on wavelengths for the two FASH mirrors, which indicates reflection bandwidths for the FH wavelength ranging from 1200 nm to 1450 nm and the SH wavelength from 630 nm to 680 nm. Reflectivity is in excess of 95% around 1310 nm and 97% around 655 nm for seven pairs, which reaches up to 99.998% and 99.999%, respectively, for 20 pairs. The parameters of LN are set to be  $d_{33} = 19.3$  pm/V,  $n_{\text{LN},\text{FH}} = 2.14$ , and  $n_{\text{LN},\text{SH}} = 2.20$ . The size for half a period of

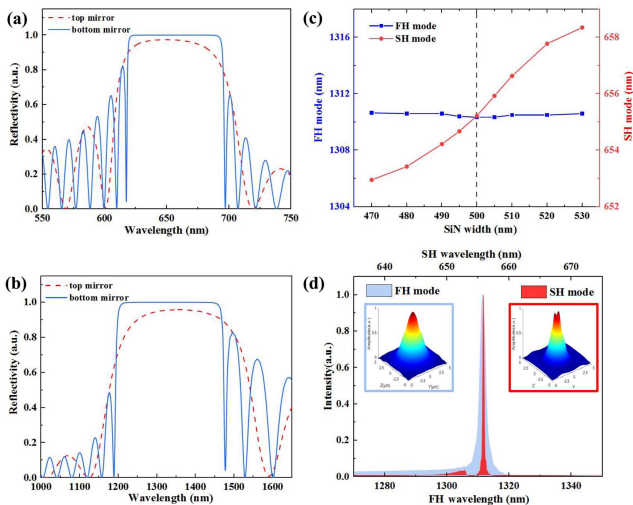


**Fig. 2.** Microcavity optimization for double resonance. (a), (b) The reflectivity of the two FASH mirrors at FH and SH wavelength, respectively; (c) effects of the changes of SiN thickness on the SH mode wavelength when the FH wavelength is fixed based on the tunability of open cavity; (d) the spectrum of FH and SH modes for  $L_{\text{air}} = 0.96 \mu\text{m}$ . The inset shows the field distributions of the output FH and SH modes just after entering the fiber.

the standing SH mode inside LN is approximately 140 nm, which would be the ideal thickness of the LN layer if the peaks of the FH and SH modes are precisely aligned. However, due to the varying reflection phases of the FH and SH waves by the FASH mirror, the peaks of FH and SH modes become misaligned. To address this, we have chosen  $H_{\text{LN}} = 100$  nm to achieve an effective nonlinear modal overlap. The SiN layer has  $n_{\text{SiN},\text{FH}} = 2.19$  and  $n_{\text{LN},\text{SH}} = 2.26$ . As shown in Fig. 2(c), the frequency matching for  $\lambda_{\text{FH}} = 1310$  nm according to Eq. (1) is satisfied for  $H_{\text{SiN}} = 500$  nm. The additional  $\text{SiO}_2$  layer is chosen to be  $H_{\text{SiO}_2} = 380$  nm for keeping both peaks of the FH and SH modes in the center of LN and maximizing the nonlinear modal overlap.

We use Lumerical finite-difference time-domain (FDTD) solutions to simulate the resonant FH and SH modes of the microcavity, in which step mesh sizes are set to 10 nm in the  $x$  axis and 25 nm in the  $y$  and  $z$  axes for obtaining sufficiently fine and accurate field distributions. A dipole with  $y$  polarization is put in the center of the LN layer to calculate spectra and  $Q$  values. A single three-dimensional simulation with such fine meshes requires tens of gigabytes for memory and a day or two for computing when the number of DBR pairs increases to more than 10. Choosing  $L_{\text{air}} = 0.96 \mu\text{m}$  that supports double resonance, Fig. 2(d) shows the spectra of the resonant FH and SH modes with central wavelengths of 1311.51 nm and 655.87 nm, respectively. The FOM is calculated to be 0.0175% based on Eq. (2), ensuring the spectrum overlap between FH and SH modes. Their optical field distributions just after entering the fiber are presented in the inset of Fig. 2(d), indicating high in-coupling of the FH field and out-coupling of the SH field. The deviation from the Gaussian shape in the SH field can be attributed to the fact that the optical fiber supports higher-order modes at SH wavelengths.

### 4. Calculations of Nonlinear Modal Overlap and $Q$ -Factors

We characterize the conversion efficiency of SHG by considering a realistic experimental realization that the FH wave couples in the microcavity from the optical fiber, while the SHG couples out reversely. In the undepleted regime, the conversion efficiency of SHG normalized to the pump power in the absence of non-radiative losses, i.e., the unit is  $\text{W}^{-1}$ , can be written as<sup>[41,42]</sup>

$$\eta = \frac{P_{\text{SH}}}{P_{\text{FH}}^2} = \frac{8}{\omega_{\text{FH}}} \left( \frac{d_{33}}{\sqrt{\epsilon_0 \lambda_{\text{FH}}}} \right)^2 |\beta|^2 Q_{r,\text{FH}}^2 Q_{r,\text{SH}} r_{c,\text{FH}}^2 r_{c,\text{SH}}, \quad (3)$$

where  $\epsilon_0$  is the permittivity of free space;  $r_{c,\text{FH}}$  and  $r_{c,\text{SH}}$  are coupling efficiencies for the FH and SH modes without considering the FASH reflection, which are determined by the modal matching between optical fields on the top FASH mirror and the optical fiber;  $Q_{r,\text{FH}}$  and  $Q_{r,\text{SH}}$  refer to the loaded  $Q$ -factors for the FH and SH waves, respectively.

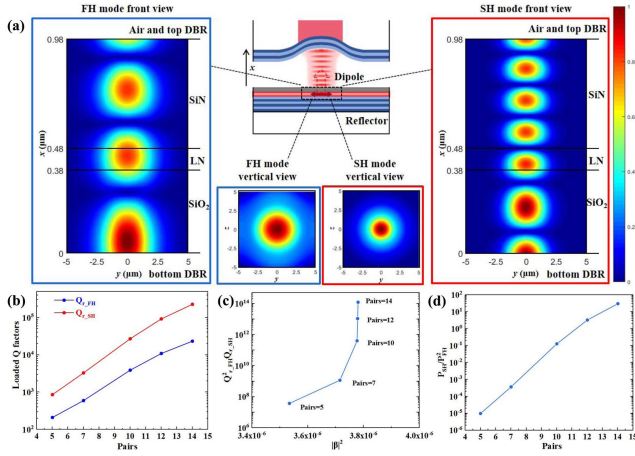


**Fig. 3.** (a) Electric field profile in front view and vertical view of the FH and SH modes; (b) loaded  $Q$ -factors of the FH mode and SH mode as functions of  $N_{\text{top}}$ ; (c) relationship between  $Q_{r\_FH}^2 Q_{r\_SH}$  and  $\beta$  with different number of  $N_{\text{top}}$ ; (d) SHG conversion efficiency as a function of  $N_{\text{top}}$ .

Figure 3(a) shows the electric field distributions inside the microcavity for both the FH and SH modes for  $L_{\text{air}} = 0.96 \mu\text{m}$ , which are obtained by adding a filter to remove the information of the source. The electric field distributions of the two modes in the LN layer show an awfully high degree of overlap through the front and vertical views. The reason why the optical field at the boundary of the bottom FASH mirror is neither the antinode nor the node is the reflection phase of the FASH mirror not being an integral multiple of  $\pi$ . The reflection phase introduces an additional phase shift that aids in the double resonance, as Eq. (1) indicated. The mode volumes of FH and SH modes are calculated to be about  $4.5(\lambda_{\text{FH}}/n)^3$  and  $13(\lambda_{\text{SH}}/n)^3$ , respectively. The mode patterns in Fig. 3(a) can be used to calculate the nonlinear overlap factor  $\beta$  that is used to characterize the nonlinear conversion efficiencies independent of  $\chi^{(2)}$  values and the FH power, which is defined as<sup>[43]</sup>

$$\beta = \frac{\lambda_{\text{FH}}^{3/2} \int dr \tilde{\epsilon}(r) E_{x\_FH}^2 E_{x\_SH}^*}{\left( \int dr \epsilon_{\text{FH}}(r) |E_{\text{FH}}|^2 \right) \left( \int dr \epsilon_{\text{SH}}(r) |E_{\text{SH}}|^2 \right)^{1/2}}, \quad (4)$$

where  $\tilde{\epsilon}(r)$  is defined to be one in the  $\chi^{(2)}$  medium and zero outside. Large  $\beta$  in the microcavity can lead to high SHG based on

Eq. (3). In Fig. 3(b), we plot the radiative  $Q$ -factors of the FH and SH modes as functions of  $N_{\text{top}}$  with  $N_{\text{bottom}} = 20$ . As expected,  $Q_{r\_FH}$  and  $Q_{r\_SH}$  increase with  $N_{\text{top}}$ . Most remarkably,  $Q_{r\_SH}$  can reach  $2.27 \times 10^5$  for  $N_{\text{top}} = 14$ , in spite of  $Q_{r\_FH} = 2.33 \times 10^4$ . Figure 3(c) shows the two important qualities for nonlinear SHG: the product of  $Q_{r\_FH}^2 Q_{r\_SH}$  and  $\beta$ .  $\beta$  can nearly reach up to  $2 \times 10^{-3}$  according to Eq. (5). Besides, the field distribution in the FP cavity is stable, and thus the  $\beta$  factor does not decline with the increase of  $Q_r$ , which enables increasing  $N_{\text{top}}$  to further improve the efficiency (see details in Table 1). The Gaussian shape in the  $y$ - $z$  plane reveals the compelling advantage of flexible in- and out-coupling of the optical field, which are calculated to be about 70% for both  $r_{c\_FH}$  and  $r_{c\_SH}$ . Clearly, the large coupling efficiency, nonlinear modal overlap, and  $Q$ -factor lead to highly efficient SHG. The conversion efficiency exceeds 0.01%/W in the general case for  $N_{\text{top}} = 7$  and goes beyond 3000%/W for  $N_{\text{top}} = 14$ , as shown in Fig. 3(d).

## 5. Robust and Tunable Double Resonance

In order to analyze the tunable and robust properties of the microcavity, we rewrite Eq. (1) as

$$\begin{cases} k_{\text{FH}} L_{\text{air}} + b_{\text{FH}} = \lambda_{\text{FH}} \\ k_{\text{SH}} L_{\text{air}} + b_{\text{SH}} = \lambda_{\text{SH}} \end{cases}, \quad (5)$$

in which the parameters are defined as the following:

$$\begin{cases} k_{\text{FH}} = \frac{4\pi n_{\text{air}}}{2\pi m_{\text{FH}} - \varphi_{\text{top,FH}} - \varphi_{\text{bottom,FH}}} \\ k_{\text{SH}} = \frac{4\pi n_{\text{air}}}{2\pi m_{\text{SH}} - \varphi_{\text{top,SH}} - \varphi_{\text{bottom,SH}}} \\ b_{\text{FH}} = \frac{4\pi(n_{\text{SiO}_2, \text{FH}} H_{\text{SiO}_2} + n_{\text{SiN, FH}} H_{\text{SiN}} + n_{\text{LN, FH}} H_{\text{LN}})}{2\pi m_{\text{FH}} - \varphi_{\text{top,FH}} - \varphi_{\text{bottom,FH}}} \\ b_{\text{SH}} = \frac{4\pi(n_{\text{SiO}_2, \text{SH}} H_{\text{SiO}_2} + n_{\text{SiN, SH}} H_{\text{SiN}} + n_{\text{LN, SH}} H_{\text{LN}})}{2\pi m_{\text{SH}} - \varphi_{\text{top,SH}} - \varphi_{\text{bottom,SH}}} \end{cases}. \quad (6)$$

The induced SiN and LN layers make the frequency-matching condition equivalent to  $m_{\text{SH}} = 2 \times m_{\text{FH}} + 2$ , directly revealed by Fig. 3(a). We plot the shifts of the FH and SH resonances by sweeping the  $L$  around  $7 \mu\text{m}$  in Fig. 4(a) based on Eq. (5). The values  $k_{\text{FH}}$  and  $b_{\text{FH}}$  can be extracted from the slope and intercept of the blue line, while  $k_{\text{SH}}$  and  $b_{\text{SH}}$  are from the red line.

**Table 1.** Main Parameters of the Fiber-Based Open Cavities with  $L_{\text{air}} = 1.94 \mu\text{m}$ .

$N_{\text{top}}$	$Q_{r\_FH}$	$Q_{r\_SH}$	$V_{\text{FH}} (\lambda/n)^3$	$V_{\text{SH}} (\lambda/n)^3$	$\beta$	$r_{c\_FH}$	$r_{c\_SH}$	$\eta (\text{W}^{-1})$
5	210	860	4.75	13.21	0.00188	0.705	0.691	$9.78 \times 10^{-4}\%$
7	596	3285	4.42	12.89	0.00193	0.733	0.735	$3.64 \times 10^{-2}\%$
10	3888	26,982	4.38	12.80	0.00194	0.729	0.735	12.80%
12	10,902	92,041	4.38	12.79	0.00194	0.715	0.725	325.60%
14	23,312	226,908	4.38	12.79	0.00194	0.671	0.674	3006.60%

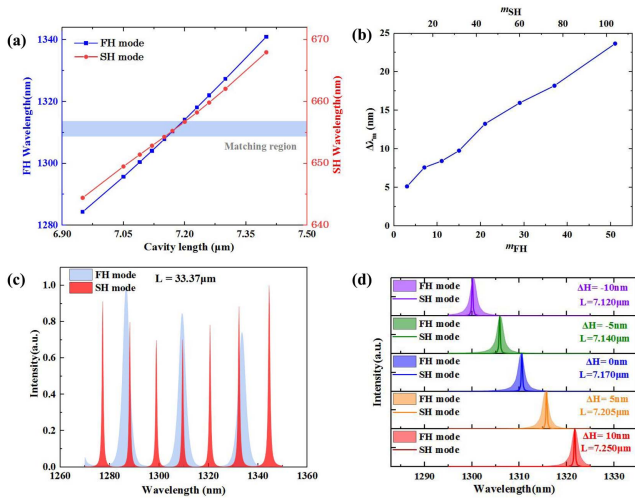


**Fig. 4.** (a) Center wavelength corresponding to the two resonant modes when the cavity length is continuously adjusted; (b) the matching bandwidth  $\Delta\lambda_m$  as a function of the longitudinal mode index  $m$ ; (c) spectrum with 33.37  $\mu\text{m}$  cavity length; (d) for different thicknesses of SiN, the corresponding wavelength achieving alignment between FH and SH waves by changing the cavity length.

Clearly,  $k_{\text{FH}}$  and  $k_{\text{SH}}$  show sensitivities of resonance wavelengths to the cavity deviation. At a small cavity length, e.g.,  $L = 7.09 \mu\text{m}$ , the resonance  $\lambda_{\text{SH}} = 1300.47 \text{ nm}$  is 2.4 nm smaller than twice that of the resonance  $\lambda_{\text{SH}} = 651.44 \text{ nm}$ . However, because the shift rate of  $k_{\text{FH}}$  is larger than  $2 \times k_{\text{SH}}$ , the critical frequency

matching is achieved by increasing  $L$ , i.e.,  $L = 7.17 \mu\text{m}$ , corresponding to  $\lambda_{\text{FH}} \approx 1310 \text{ nm}$  and  $\lambda_{\text{SH}} \approx 655 \text{ nm}$ . In order to numerically characterize the robustness, we define the matching bandwidth of  $\Delta\lambda_m$  referring to the tunable FH wavelength range versus the cavity lengths when the center wavelength of the SH spectra keeps inside the half-maximum of the FH spectra. Clearly, the robustness to the cavity length depends on the  $Q$ -factor and the smaller value of  $k_{\text{FH}} - 2 \times k_{\text{SH}}$ . As a demonstration, we choose  $N_{\text{top}} = 7$  to get a smaller  $Q_{r,\text{FH}} = 600$ , corresponding to a resonant bandwidth up to 2 nm. According to Eq. (5),  $k_{\text{FH}}$  and  $k_{\text{SH}}$  will become closer for larger cavity length, resulting in a large matching bandwidth for double resonance, supported by the simulated results in Fig. 4(b). Therefore, a longer cavity is more robust to cavity length deviation. It should be noted that the longitudinal mode indexes  $m_{\text{FH}}$  and  $m_{\text{SH}}$  increase linearly with the cavity length. With a larger cavity length such as 33.37  $\mu\text{m}$ , more than one cavity mode can satisfy double resonance, as shown in Fig. 4(c), which further broadens the operating wavelength for the microcavity. However, precise re-alignment of FH and SH resonance at other wavelengths in Fig. 4(c) requires additional material dispersion based on Eqs. (5) and (6), which can be realized by changing the thickness of the SiN layer along with  $L$ . The mature chemical vapor deposition technique used for depositing the SiN layer enables convenient control over its thickness during the fabrication process. As shown in Fig. 4(d), the double resonance can be tuned from  $\lambda_{\text{FH}} = 1300 \text{ nm}$  to 1320 nm, corresponding to  $\lambda_{\text{SH}} = 650 \text{ nm}$  to 660 nm, via thickness variation of about 20 nm for the SiN layer and total cavity length variation of about 130 nm. These robust

**Table 2.** Different Structures of Double Resonances.

Ref.	Structure	$\beta$	$Q_{r,\text{FH}}/Q_{r,\text{SH}}$	$\lambda_{\text{SH}}$ (nm)	Processing Difficulty	Coupling Approach
[14] <sup>a</sup>	AlGaAs/Al <sub>2</sub> O <sub>3</sub> micropillar	0.018	5000/1000	Single, 750	Challenging (irregular)	Free space
[15] <sup>b</sup>	LN WGM resonator	0.00001	$3.4 \times 10^7/-$	Single, 532	Etching	Free space
[44] <sup>a</sup>	AlGaAs nanoring	0.004	$10^4/>10^6$	Single, 775	Etching	Waveguide
[43] <sup>a</sup>	AlGaAs PhC	0.01	$3.6 \times 10^4/1100$	Single, 775	Challenging (etching, careful optimization)	Free space
	Al <sub>0.3</sub> Ga <sub>0.7</sub> As PhC	0.0035	$1.1 \times 10^5/400$	Single, 775		Free space
[41] <sup>a</sup>	GaN PhC	$\sim 0.005$	$10^5/10^4$	Single, 650	Etching	Free space
[37] <sup>a</sup>	ZnO PhC	0.001	$3 \times 10^5/2.95 \times 10^6$	Single, 376	Etching	Free space
[45] <sup>a</sup>	GaAs PhC nanobeam	0.00021	$10^6/4000$	Single, 910	Etching	Free space
		0.00012	$6 \times 10^4/4000$	Single, 910	Etching	Free space
[33] <sup>b</sup>	MoS <sub>2</sub> FP cavity	-	77/46	Single, 462	No etching	Free space
Our work <sup>a</sup>	LN FP open cavity (short length)	0.002	$2.33 \times 10^4/2.27 \times 10^5$	Single, 655	No etching	Fiber
	LN FP open cavity (long length)	0.0001	600/3300	Tunable, 652-660	No etching	Fiber

<sup>a</sup>Calculation results.  
<sup>b</sup>Experimental results.

and tunable properties provide a flexible way to construct a doubly resonant microcavity working at different wavelengths and support a pulsed FH beam to excite the SHG signal for further increasing the efficiency.

## 6. Conclusion

In conclusion, we have numerically and theoretically studied a simple but promising approach to achieving doubly resonant SHG via a high- $Q$  fiber-based tunable FP microcavity combined with different thin films to achieve large nonlinear modal overlap and frequency matching. The conversion efficiency of SHG up to  $3000\% W^{-1}$  is obtained for high-reflectivity FASH mirrors and smaller modal volume, while widely tunable and robust double resonance is achieved by increasing the cavity length along with changing the SiN thickness. By comparison, the designed microcavity possesses the efficiency of SHG  $10^9$  times the reported result of  $1.68 \times 10^{-6}\% W^{-1}$  in the FP cavity<sup>[33]</sup> and provides wide tunability for the cavity operating wavelength relative to all other resonant schemes (see details in Table 2). Since no etching process is required to fabricate micro structures on the LN and SiN layers, and they exhibit minimal absorption loss at the designed wavelength, the main factors that can potentially degrade the conversion efficiency in a practical device are the FASH mirrors and the nonlinear modal overlap factor. On one hand, it is challenging to fabricate the FASH mirrors that provide high reflectivity for both the FH and SH waves, resulting in a smaller  $Q$ -factor. On the other hand, any thickness deviation in the LN and SiN layers can impact the nonlinear modal overlap in the LN layer and lead to a decrease in the conversion efficiency. This easily constructed microcavity will promote the practical realization of second-order nonlinear processes with unprecedented conversion efficiency and large tunability for the generation of tunable laser sources and high-quality quantum sources. Moreover, by substituting the nonlinear layer with materials featuring two-level or three-level systems, and strategically tailoring the multiple resonances to coincide with excitation and emission spectra, a promising avenue emerges for the realization of highly efficient solid-state single-photon sources, nonlinear optical parametric polaritons, or microlasers<sup>[46-50]</sup>. This approach holds the potential to enhance the performance and functionality of such devices in solid-state systems.

## Acknowledgement

This work was supported by the National Key R&D Program of China (2021YFA1400803), the National Natural Science Foundation of China (No. 12204019), the China Postdoctoral Science Foundation (No. 2022M710233), and the National Postdoctoral Program for Innovative Talents (No. BX20220010).

## References

1. X. Han, W. Fu, C. L. Zou, L. Jiang, and H. X. Tang, "Microwave-optical quantum frequency conversion," *Optica* **8**, 1050 (2021).
2. K. Koshelev, S. Kruk, E. Melik-Gaykazyan, J. H. Choi, A. Bogdanov, H. G. Park, and Y. Kivshar, "Subwavelength dielectric resonators for nonlinear nanophotonics," *Science* **367**, 288 (2020).
3. J. Y. Wang, Z. J. Liu, J. Xiang, B. Chen, Y. M. Wei, W. J. Liu, Y. Xu, S. Lan, and J. Liu, "Ultraviolet second harmonic generation from Mie-resonant lithium niobate nanospheres," *Nanophotonics* **10**, 4273 (2021).
4. Z. Ma, J. Y. Chen, Z. Li, C. Tang, Y. M. Sua, H. Fan, and Y. P. Huang, "Ultrabright quantum photon sources on chip," *Phys. Rev. Lett.* **125**, 263602 (2020).
5. J. Liu, F. Bo, L. Chang, C. H. Dong, X. Ou, B. Regan, X. Q. Shen, Q. H. Song, B. C. Yao, W. F. Zhang, C. L. Zou, and Y. F. Xiao, "Emerging material platforms for integrated microcavity photonics," *Sci. China Phys. Mech. Astron.* **65**, 104201 (2022).
6. G. P. Lin, A. Coillet, and Y. K. Chembo, "Nonlinear photonics with high- $Q$  whispering-gallery-mode resonators," *Adv. Opt. Photonics* **9**, 828 (2017).
7. X. Zhang, Q.-T. Cao, Z. Wang, Y.-X. Liu, C.-W. Qiu, L. Yang, Q. Gong, and Y.-F. Xiao, "Symmetry-breaking-induced nonlinear optics at a microcavity surface," *Nat. Photonics* **13**, 21 (2019).
8. J. Chen, X. Shen, S. J. Tang, Q. T. Cao, Q. Gong, and Y. F. Xiao, "Microcavity nonlinear optics with an organically functionalized surface," *Phys. Rev. Lett.* **123**, 173902 (2019).
9. Z. T. Li, L. D. Zhou, Z. J. Liu, M. C. Panmai, S. L. Li, J. Liu, and S. Lan, "Modifying the quality factors of the bound states in the continuum in a dielectric metasurface by mode coupling," *ACS Photonics* **10**, 206 (2023).
10. Z. J. Liu, Y. Xu, Y. Lin, J. Xiang, T. H. Feng, Q. T. Cao, J. T. Li, S. Lan, and J. Liu, "High- $Q$  quasibound states in the continuum for nonlinear metasurfaces," *Phys. Rev. Lett.* **123**, 253901 (2019).
11. P. Vabishchevich and Y. Kivshar, "Nonlinear photonics with metasurfaces," *Photonics Res.* **11**, B50 (2023).
12. B. Fang, H. M. Li, S. N. Zhu, and T. Li, "Second-harmonic generation and manipulation in lithium niobate slab waveguides by grating metasurfaces," *Photonics Res.* **8**, 1296 (2020).
13. A. Rodriguez, M. Soljačić, J. D. Joannopoulos, and S. G. Johnson, " $\chi^{(2)}$  and  $\chi^{(3)}$  harmonic generation at a critical power in inhomogeneous doubly resonant cavities," *Opt. Express* **15**, 7303 (2007).
14. Z. Lin, X. D. Liang, M. Lončar, S. G. Johnson, and A. W. Rodriguez, "Cavity-enhanced second-harmonic generation via nonlinear-overlap optimization," *Optica* **3**, 233 (2016).
15. J. U. Fürst, D. V. Strelakov, D. Elser, M. Lassen, U. L. Andersen, C. Marquardt, and G. Leuchs, "Naturally phase-matched second-harmonic generation in a whispering-gallery-mode resonator," *Phys. Rev. Lett.* **104**, 153901 (2010).
16. Y. F. Xiao, C. L. Zou, B. B. Li, Y. Li, C. H. Dong, Z. F. Han, and Q. H. Gong, "High- $Q$  exterior whispering-gallery modes in a metal-coated microresonator," *Phys. Rev. Lett.* **105**, 153902 (2010).
17. J. T. Lin, N. Yao, Z. Z. Hao, J. H. Zhang, W. B. Mao, M. Wang, W. Chu, R. B. Wu, Z. W. Fang, L. L. Qiao, W. Fang, F. Bo, and Y. Cheng, "Broadband quasi-phase-matched harmonic generation in an on-chip monocrytalline lithium niobate microdisk resonator," *Phys. Rev. Lett.* **122**, 173903 (2019).
18. Q. T. Cao, H. Wang, C. H. Dong, H. Jing, R. S. Liu, X. Chen, L. Ge, Q. Gong, and Y. F. Xiao, "Experimental demonstration of spontaneous chirality in a nonlinear microresonator," *Phys. Rev. Lett.* **118**, 033901 (2017).
19. Z. Z. Hao, L. Zhang, W. B. Mao, A. Gao, X. M. Gao, F. Gao, F. Bo, G. Q. Zhang, and J. J. Xu, "Second-harmonic generation using  $d_{33}$  in periodically poled lithium niobate microdisk resonators," *Photonics Res.* **8**, 311 (2020).
20. X. Jiang, L. Shao, S. X. Zhang, X. Yi, J. Wiersig, L. Wang, Q. H. Gong, M. Loncar, L. Yang, and Y. F. Xiao, "Chaos-assisted broadband momentum transformation in optical microresonators," *Science* **358**, 344 (2017).
21. M. G. Vazimali and S. Fathpour, "Applications of thin-film lithium niobate in nonlinear integrated photonics," *Adv. Photonics* **4**, 034001 (2022).
22. J. Lu, J. B. Surya, X. Liu, A. W. Bruch, Z. Gong, Y. Xu, and H. X. Tang, "Periodically poled thin-film lithium niobate microring resonators with a second-harmonic generation efficiency of 250,000%/W," *Optica* **6**, 1455 (2019).

23. R. Luo, Y. He, H. Liang, M. Li, J. Ling, and Q. Lin, "Optical parametric generation in a lithium niobate microring with modal phase matching," *Phys. Rev. Appl.* **11**, 034026 (2019).
24. J.-Y. Chen, Z.-H. Ma, Y. M. Sua, Z. Li, C. Tang, and Y.-P. Huang, "Ultra-efficient frequency conversion in quasi-phase-matched lithium niobate microrings," *Optica* **6**, 1244 (2019).
25. Z. Liu, J. Wang, B. Chen, Y. Wei, W. Liu, and J. Liu, "Giant enhancement of continuous wave second harmonic generation from few-layer GaSe coupled to high-Q quasi bound states in the continuum," *Nano Lett.* **21**, 7405 (2021).
26. G. Qiu, D. Wei, Z. Liu, and J. Liu, "Enhancement of spontaneous emission from CdSe/ZnS quantum dots through silicon nitride photonic crystal cavity based on miniaturized bound states in the continuum," *Nanoscale* **15**, 3757 (2023).
27. J. Wang, M. Clementi, M. Minkov, A. Barone, J.-F. Carlin, N. Grandjean, D. Gerace, S. Fan, M. Galli, and R. Houdré, "Doubly resonant second-harmonic generation of a vortex beam from a bound state in the continuum," *Optica* **7**, 1126 (2020).
28. J.-Y. Chen, C. Tang, Z.-H. Ma, Z. Li, Y. M. Sua, and Y.-P. Huang, "Efficient and highly tunable second-harmonic generation in Z-cut periodically poled lithium niobate nanowaveguides," *Opt. Lett.* **45**, 3789 (2020).
29. E. Nitiss, O. Yakar, A. Stroganov, and C.-S. Brès, "Highly tunable second-harmonic generation in all-optically poled silicon nitride waveguides," *Opt. Lett.* **45**, 1958 (2020).
30. R. Luo, Y. He, H. Liang, M. Li, and Q. Lin, "Highly tunable efficient second-harmonic generation in a lithium niobate nanophotonic waveguide," *Optica* **5**, 1006 (2018).
31. F. Li, Y. Li, Y. Cai, P. Li, H. Tang, and Y. Zhang, "Tunable open-access microcavities for solid-state quantum photonics and polaritonics," *Adv. Quantum Technol.* **2**, 1900060 (2019).
32. R. Albrecht, A. Bommer, C. Deutsch, J. Reichel, and C. Becher, "Coupling of a single nitrogen-vacancy center in diamond to a fiber-based microcavity," *Phys. Rev. Lett.* **110**, 243602 (2013).
33. F. Yi, M. Ren, J. C. Reed, H. Zhu, J. Hou, C. H. Naylor, A. C. Johnson, R. Agarwal, and E. Cubukcu, "Optomechanical enhancement of doubly resonant 2D optical nonlinearity," *Nano Lett.* **16**, 1631 (2016).
34. H. Kelkar, D. Wang, D. Martín-Cano, B. Hoffmann, S. Christiansen, S. Götzinger, and V. Sandoghdar, "Sensing nanoparticles with a cantilever-based scannable optical cavity of low finesse and sub- $\lambda^3$  volume," *Phys. Rev. Appl.* **4**, 054010 (2015).
35. V. Berger, "Second-harmonic generation in monolithic cavities," *J. Opt. Soc. Am. B* **14**, 1351 (1997).
36. M. Liscidini and L. C. Andreani, "Second-harmonic generation in doubly resonant microcavities with periodic dielectric mirrors," *Phys. Rev. E* **73**, 016613 (2006).
37. J. A. Medina-Vázquez, E. Y. González-Ramírez, and J. G. Murillo-Ramírez, "Photonic crystal meso-cavity with double resonance for second-harmonic generation," *J. Phys. B At. Mol. Opt. Phys.* **54**, 245401 (2021).
38. X. Li, J. Ma, S. Liu, P. Huang, B. Chen, D. Wei, and J. Liu, "Efficient second harmonic generation by harnessing bound states in the continuum in semi-nonlinear etchless lithium niobate waveguides," *Light Sci. Appl.* **11**, 317 (2022).
39. J. Lin, F. Bo, Y. Cheng, and J. Xu, "Advances in on-chip photonic devices based on lithium niobate on insulator," *Photonics Res.* **8**, 1910 (2020).
40. P. Qing, J. Gong, X. Lin, N. Yao, W. Shen, A. Rahimi-Iman, W. Fang, and L. Tong, "A simple approach to fiber-based tunable microcavity with high coupling efficiency," *Appl. Phys. Lett.* **114**, 021106 (2019).
41. M. Minkov, D. Gerace, and S. Fan, "Doubly resonant  $\chi^{(2)}$  nonlinear photonic crystal cavity based on a bound state in the continuum," *Optica* **6**, 1039 (2019).
42. A. D. Logan, M. Gould, E. R. Schmidgall, K. Hestroffer, Z. Lin, W. Jin, A. Majumdar, F. Hatami, A. W. Rodriguez, and K.-M. C. Fu, "400%/W second harmonic conversion efficiency in 14  $\mu\text{m}$ -diameter gallium phosphide-on-oxide resonators," *Opt. Express* **26**, 33687 (2018).
43. S. Zanotti, M. Minkov, S. Fan, L. C. Andreani, and D. Gerace, "Doubly-resonant photonic crystal cavities for efficient second-harmonic generation in III-V semiconductors," *Nanomaterials* **11**, 605 (2021).
44. Z.-F. Bi, A. W. Rodriguez, H. Hashemi, D. Duchesne, M. Loncar, K.-M. Wang, and S. G. Johnson, "High-efficiency second-harmonic generation in doubly-resonant  $\chi^{(2)}$  microring resonators," *Opt. Express* **20**, 7526 (2012).
45. S. Buckley, M. Radulaski, J. L. Zhang, J. Petykiewicz, K. Biermann, and J. Vuckovic, "Multimode nanobeam cavities for nonlinear optics: high quality resonances separated by an octave," *Opt. Express* **22**, 26498 (2014).
46. Y. Wei, S. Liu, X. Li, Y. Yu, X. Su, S. Li, X. Shang, H. Liu, H. Hao, H. Ni, S. Yu, Z. Niu, J. Iles-Smith, J. Liu, and X. Wang, "Tailoring solid-state single-photon sources with stimulated emissions," *Nat. Nanotechnol.* **17**, 470 (2022).
47. J. Zhao, A. Fieramosca, R. Bao, W. Du, K. Dini, R. Su, J. Feng, Y. Luo, D. Sanvitto, T. C. H. Liew, and Q. Xiong, "Nonlinear polariton parametric emission in an atomically thin semiconductor based microcavity," *Nat. Nanotechnol.* **17**, 396 (2022).
48. H. Tang, Y. Wang, Y. Chen, K. Wang, X. He, C. Huang, S. Xiao, S. Yu, and Q. Song, "Ultra-high-Q lead halide perovskite microlasers," *Nano Lett.* **23**, 3418 (2023).
49. X. Zhou, L. Zhai, and J. Liu, "Epitaxial quantum dots: a semiconductor launchpad for photonic quantum technologies," *Photon. Insights* **1**, R07 (2023).
50. S. Liu, Y. Wei, X. Li, Y. Yu, J. Liu, S. Yu, and X. Wang, "Dual-resonance enhanced quantum light-matter interactions in deterministically coupled quantum-dot-micropillars," *Light Sci. Appl.* **10**, 158 (2021).